International Journal of Computer Vision

DOI: 10.1007/s11263-007-0036-1

Appearance Sampling of Real Objects for Variable Illumination

IMARI SATO*
National Institute of Informatics
imarik@nii.ac.jp

TAKAHIRO OKABE AND YOICHI SATO
The University of Tokyo
takahiro@iis.u-tokyo.ac.jp
ysato@iis.u-tokyo.ac.jp

Received May 1, 2006; Accepted January 2, 2007

Abstract. The appearance of an object greatly changes under different lighting conditions. Even so, previous studies have demonstrated that the appearance of an object under varying illumination conditions can be represented by a linear subspace. A set of basis images spanning such a linear subspace can be obtained by applying the principal component analysis (PCA) for a large number of images taken under different lighting conditions. Since little is known about how to sample the appearance of an object in order to correctly obtain its basis images, it was a common practice to use as many input images as possible. In this study, we present a novel method for analytically obtaining a set of basis images of an object for varying illumination from input images of the object taken properly under a set of light sources, such as point light sources or extended light sources. Our proposed method incorporates the sampling theorem of spherical harmonics for determining a set of lighting directions to efficiently sample the appearance of an object. We further consider the issue of aliasing caused by insufficient sampling of the object's appearance. In particular, we investigate the effectiveness of using extended light sources for modeling the appearance of an object under varying illumination without suffering the aliasing caused by insufficient sampling of its appearance.

Keywords: physics-based computer vision, image-based modeling and rendering, reflectance analysis

1. Introduction

It is well known that the appearance of an object significantly changes under different illumination conditions. For instance, the change in appearance of someone's face often becomes much larger than the difference between two different faces under the same lighting. For the object recognition and image synthesis task, it is thus important to be able to predict the variation of an object's appearance under varying illumination conditions.

While there may seem to be a large variety of possible appearances for a given object, previous research has demonstrated that the appearance changes of an object under varying illumination can be represented with a linear subspace spanned by a set of basis images of the object. For instance, for a convex Lambertian object, its appearance seen under distant illumination without attached and cast shadows can be described with a 3-D linear subspace spanned from three input images of the object taken under linearly independent lighting conditions (Murase and Nayar, 1995; Shashua, 1997; Zhao and Yang, 1999).

Even when taking attached shadows into account, most of the image variations of a human face or other object under varying illumination was shown to be adequately represented by a low-dimensional linear subspace slightly higher than 3-D (Hallinan, 1994; Epstein et al., 1995; Yuille et al., 1999). Hallinan reported: (a) that a 5-D

*Corresponding author.

subspace would suffice to represent most of the image variations due to illumination changes, including extreme cases where a face is lit from its sides, and (b) that a 3-D subspace would be sufficient when a face is lit mainly from its front (Hallinan, 1994). Georghiades et al. used a similar observation more specifically for object recognition under varying lighting conditions (Georghiades et al., 1998, 2001).

A set of basis images spanning such a linear subspace are often provided by applying a principal-component analysis (PCA) to the input images of an object taken under different lighting conditions.[1] Since little is known about how to sample the appearance of an object in order to correctly obtain its basis images, a large number of input images taken by moving a point light source along a sphere surrounding the object are generally provided.

Another interesting observation from Hallinan's early work is that a subspace obtained by PCA does not vary widely between sparsely and densely sampled sets of lighting directions for faces (Hallinan, 1994). However, it was not known how many images would be sufficient to correctly obtain the basis images. Then one might ask whether a certain set of input images of an object would be sufficient to fully span the subspace of the object for arbitrary illumination conditions or whether the use of a point light source is suitable for capturing the variation in the object's appearance. Previous empirical studies do not necessarily provide enough insight into this important question, and thus it has been a common practice to use as many input images as possible to ensure that the set of input images spans a subspace entirely.

Recent investigations into the frequency-space analysis of reflection have shown that the appearance of an object under varying complex illumination conditions can be well represented with a linear subspace spanned by basis images of the object, called *harmonic images*, each of which corresponds to an image of the object illuminated under *harmonic lights* whose distributions are specified in terms of spherical harmonics (Ramamoorthi and Hanrahan, 2001a,b; Basri and Jacobs, 2001).[2] Therefore, if harmonic lights can be physically constructed in a real setting, harmonic images of a real object can be obtained simply as images of the object seen under these light sources.

However, harmonic lights are complex diffuse light sources comprising both negative and positive radiance and are thus difficult to physically construct in a real setting. Therefore, most of the previously proposed techniques synthetically compute harmonic images from the knowledge of an object's 3-D shape and reflectance properties. This motivates us to develop a method for determining a set of harmonic images of a real object by using only the input images of the object under simple lighting, such as a point light source.

There have been several methods that make use of prior knowledge about objects for efficiently obtaining their basis images. For instance, Lee et al. introduced the interesting concept of object classes for determining a configuration of nine light source directions. Input images taken under those particular light source directions approximate a 9-D subspace spanned by harmonic images (Lee et al., 2001). This method has the advantage in that it requires only synthetically provided harmonic images for one object in each class in order to determine the nine lighting directions.

Shim and Chen introduced an approach that used training scenes with different shapes and surface materials for finding the most efficient lighting patterns to model the appearance changes of an object (Shim and Chen, 2004). Zhang and Samaras employed a statistical model of harmonic images of human faces for obtaining harmonic images of a person from his or her single image (Zhang and Samaras, 2003). Those approaches, however, require additional images or prior knowledge about the 3-D shapes and reflectance properties of one or more objects in each object class.

In this study, we present a novel method for analytically obtaining a set of basis images of an object for variable illumination from input images of the object taken under a point light source. We show that a set of lighting directions can be determined for sampling images of an object depending on the spectrum of the object's bidirectional reflectance distribution function (BRDF) in the angular frequency domain, such that a set of harmonic images can be analytically obtained based on the sampling theorem on spherical harmonics (Driscoll and Healy, 1994).

Using those sampling directions determined from the sampling theorem, we are able to obtain harmonic images by using a significantly smaller number of input images than other techniques that do not take into account the relationship between a spectrum of BRDFs and the sampling density of the illumination directions.

We further consider the issue of the aliasing caused by insufficient sampling of an object's appearance. Although our proposed method based on the sampling theorem does not require the shape and reflectance model of an object used for synthetically rendering the harmonics images of the object, it still requires information on the highest frequency that the appearance of an object contains in order to determine the number of point light sources that are required. The sampling theorem states that the higher the frequency content of an object's appearance, the more input images are required to obtain a correct set of basis images. Accordingly, the number of input images required may become extremely large for highly specular surfaces containing a large quantity of high frequency components in their reflection. If there is an insufficient sampling of an object's appearance, aliasing will occur in the obtained basis images, and this will

lead to undesirable artifacts in the synthesized appearance.

To cope with this problem, we investigate the effectiveness of using another type of light source, Extended Light Sources *(ELS)*, for modeling the appearance of an object under varying illumination. The use of ELS for modeling the shape and reflectance of an object was originally introduced by Nayar et al. (1990), which is one of a series of pioneering color and reflectance analyses provided by Professor Kanade's research group at the Robotics Institute, Carnegie Mellon University. We further extend their analysis and combine the ELS frequency analysis with the sampling theorem on spherical harmonics, such that the harmonic images of an object of arbitrary surface materials can be obtained without suffering the aliasing caused by insufficient sampling of its appearance.

The use of ELS has the following advantages: (1) ELS has a radiance distribution that is similar to that of the Gaussian function, and this enables ELS to function as a low-pass filters when the appearance of an object is sampled under them, and (2) ELS can reduce the high contrast in image intensities due to specular and diffuse reflection components. This helps avoid saturation, so that we are able to observe both specular and diffuse reflection components in the same image taken with a single shutter speed. We have tested our proposed approach based on ELS with objects of complex appearances that are generally difficult to model using image-based modeling techniques.

The rest of this paper is organized as follows. We briefly review the harmonic image representation in Section 2. We discuss the difficulties of obtaining the harmonic images of real objects and present our approach based on the sampling theorem of spherical harmonics in Section 3. Then we consider the issues in obtaining harmonic images of real objects from images taken under a point light source and show experimental results in Section 4. We further investigate the issue of aliasing caused by insufficient sampling of an object's appearance in Section 5 and present an anti-aliasing framework for obtaining a set of correct basis images from input images taken under ELS in Section 6. Finally, we show our experimental results of the proposed method applied to synthetic and real data in Section 7 and present our concluding remarks in Section 8. This paper is an expanded and more detailed version of the works we presented in Sato et al. (2003, 2005).

2. Set of Basis Images for Variable Illumination

2.1. Review of Spherical Harmonics

Spherical Harmonics define an orthonormal basis over a unit sphere. Consider the unit sphere in R^3, a unit vector

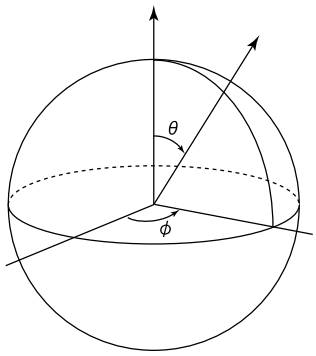

Figure 1. The polar coordinate system: θ, $(0 \leq \theta \leq \pi)$ in elevation and ϕ, $(0 \leq \phi < 2\pi)$ in azimuth.

on the sphere can be described by the polar coordinate system θ, $(0 \leq \theta \leq \pi)$ in elevation and ϕ, $(0 \leq \phi < 2\pi)$ in azimuth (Fig. 1). In this coordinate system, spherical harmonics $Y_l^m(\theta, \phi)$, $(l \geq 0, -l \leq m \leq l)$ are defined as

$$Y_l^m(\theta, \phi) = N_l^m P_l^m(\cos\theta) e^{Im\phi}, \tag{1}$$

where N_l^m are the normalized constants, and $P_l^m(\cdot)$ are the associated Legendre functions of degree l and order m.

A function $f(\theta, \phi)$ defined over the unit sphere is expanded as a linear combination of spherical harmonics as

$$f(\theta, \phi) = \sum_{l=0}^{\infty} \sum_{m=-l}^{l} f_l^m Y_l^m(\theta, \phi), \tag{2}$$

and f_l^m denotes the coefficients in its spherical harmonic expansion[3]:

$$f_l^m = \int_0^{2\pi} \int_0^{\pi} f(\theta, \phi) Y_l^m(\theta, \phi) \sin\theta d\theta d\phi. \tag{3}$$

2.2. Representing Object Appearance Based on Spherical Harmonics

A bidirectional reflectance distribution function $\rho(\theta_i', \phi_i', \theta_o', \phi_o')$ characterizes the reflectance property of an object: (θ_i', ϕ_i') and (θ_o', ϕ_o') are the incident and reflection directions with respect to the surface normal of the object's surface whose local coordinate is denoted by using $'$. For the sake of simplicity we define a transfer function $\tilde{\rho}(\theta_i', \phi_i', \theta_o', \phi_o') = \rho(\theta_i', \phi_i', \theta_o', \phi_o') \cos\theta_i'$.

Representing light source distribution $L(\theta, \phi)$ by the global coordinate defined on the unit sphere, the

brightness of the object surface is computed as

$$I = \int_0^{\pi} \int_0^{2\pi} L(\theta, \phi)\tilde{\rho}(M(\theta, \phi), \theta'_o, \phi'_o) \sin\theta \mathrm{d}\theta \mathrm{d}\phi, \quad (4)$$

where $M(\cdot)$ represents a rotation operator that rotates (θ, ϕ) into the local coordinate.

Considering the appearance changes of an object under variable illumination seen from a fixed viewpoint (θ'_o, ϕ'_o), $\tilde{\rho}(M(\theta, \phi), \theta'_o, \phi'_o)$ can be represented by using a global coordinate $R(\theta, \phi)$. In other words, $R(\theta, \phi)$ represents how much incident light from direction(θ, ϕ) is reflected on the object's surface toward the fixed viewpoint (θ'_o, ϕ'_o). In the following, $R(\theta, \phi)$ is referred to as the *reflection kernel*.

Since both the light source distribution and the reflection kernel are functions defined on the unit sphere, we can represent them as

$$L(\theta, \phi) = \sum_{l=0}^{\infty} \sum_{m=-l}^{l} L_l^m Y_l^m(\theta, \phi) \quad (5)$$

$$R(\theta, \phi) = \sum_{l=0}^{\infty} \sum_{m=-l}^{l} R_l^m Y_l^m(\theta, \phi), \quad (6)$$

where L_l^m and R_l^m are the coefficients in their spherical harmonic expansion from definition in Eq. (3):

$$L_l^m = \int_0^{2\pi} \int_0^{\pi} L(\theta, \phi) Y_l^m(\theta, \phi) \sin\theta d\theta d\phi \quad (7)$$

$$R_l^m = \int_0^{2\pi} \int_0^{\pi} R(\theta, \phi) Y_l^m(\theta, \phi) \sin\theta d\theta d\phi. \quad (8)$$

Assuming the spherical light sources with $Y_l^m(\theta, \phi)$ radiance in its (θ, ϕ) direction in Eq. (8), R_l^m represents the brightness seen under these spherical light sources called harmonic lights.

From Eqs. (5) and (6), and the orthonormality of spherical harmonics, the surface brightness I in Eq. (4) is computed in terms of L_l^m and R_l^m as

$$I = \sum_{l=0}^{\infty} \sum_{m=-l}^{l} L_l^m R_l^m. \quad (9)$$

Images containing R_l^m for all pixels, that is, for all corresponding points on the object's surface, are called harmonic images (Basri and Jacobs, 2001).

3. Methods for Obtaining Harmonic Images

There are several approaches for obtaining the harmonic images of an object. One approach is to provide a reflection kernel $R(\theta, \phi)$ of the object from the knowledge of its 3D shape and reflectance properties. Since $Y_l^m(\theta, \phi)$ are predefined functions, R_l^m are computed from Eq. (8). Most of the previously proposed methods employed this approach to synthetically compute harmonic images.

One might think of observing an object under physically constructed harmonic lights. In this case, each pixel value directly corresponds to coefficients R_l^m, and thus the 3D shapes and reflectance properties of the object need not to be given a priori. However, as pointed out by other researchers (Basri and Jacobs, 2001; Lee et al., 2001), harmonic lights are complex diffuse lighting consisting of both negative and positive radiance. It is difficult to physically construct such lighting in a real setting.

In this work, we take an alternative approach of observing a reflection kernel $R(\theta, \phi)$ for each surface point on an object directly, by taking an image of the object under a point light source located at the direction (θ, ϕ). This approach is based on the assumption that the point light source used in this method is sufficiently distant from the objects, and thus this light source projects parallel rays onto the object's surface.

The reflectance kernel $R(\theta, \phi)$ represents the radiance of the reflected light due to incoming light with a unit radiance from the direction (θ, ϕ). Therefore, if we suppose that this point light source has unit radiance, the value of $R(\theta, \phi)$ can be obtained simply as the observed brightness of the surface point when the object is illuminated under a light source from the direction (θ, ϕ).[4] Once we determine the values of $R(\theta, \phi)$ for all directions, we can compute pixel values of harmonic images as R_l^m from Eq. (8). In this way, we do not need to synthetically compute the reflection kernel $R(\theta, \phi)$ of the object, nor are the 3D shapes and reflectance properties of the object required.

Since the function $R(\theta, \phi)$ is continuously distributed on the unit sphere in Eq. (8), we first need to approximate its distribution by a discrete set of function $R(\theta, \phi)$, so that we can sample $R(\theta, \phi)$ using a point light source physically located at (θ, ϕ) direction. Then, the question we have to ask is how densely $R(\theta, \phi)$ needs to be sampled in order to correctly compute R_l^m coefficients from them. In other words, we want to know how densely a point light source needs to be positioned around an object to correctly obtain harmonics images of the object. In the next section, we will consider this issue in terms of the characteristics of spherical harmonics $Y_l^m(\theta, \phi)$.

3.1. Sampling Theorem on Spherical Harmonics Transformation

There have been several methods proposed in the field of applied mathematics to efficiently compute coefficients of a function in its spherical harmonic expansion using fewer samplings of the function. Most of these

methods discretize functions on the sphere using rectangular tessellations with different angular resolutions.

It should be noted that various approaches are also available to discretize and analyze functions on the sphere using icosahedral, triangular and curvilinear tessellations. For instance, node directions of a geodesic dome constructed based on the icosahedron are often used for uniform sampling of BRDF and illumination (Nayar et al., 1990; Nishino et al., 2001). The recently proposed Hierarchical Equal Area and isoLatitute Pixelisation (HEALPix) offers a hierarchical curvilinear tessellation at sufficiently high resolution that is suitable for fast and accurate statistical analysis of massive data (http://healpix.jpl.nasa.gov/,). In contrast to uniform sampling, spherical wavelets have good localization properties and therefore are effective in representing multi-scale structures on the sphere (Schroder and Sweldens, 1995), e.g., phenomena of different scales at different locations, while spherical harmonics composed of global waves are efficient in representing functions on the sphere localized in the frequency domain.

In this section, we adapt the sampling theorem of spherical harmonics to compute harmonic images using fewer input images of objects taken by moving a point light source to particular locations. The sampling theorem further enables us to analyze what kinds of artifacts we should expect when samplings of the reflection kernel of an object are insufficient.

It is common knowledge that the sampling theorem on the 1D line tells us that a band-limited function can be accurately reconstructed from properly sampled discrete data. Namely, Fourier coefficients of the function can be determined by weighted sums of the function sampled at even intervals. For a function defined on the sphere, a similar theorem, the sampling theorem on the sphere, has been proved (Driscoll and Healy, 1994). In this section, we outline the theorem.

Let us assume that the reflection kernel $R(\theta, \phi)$ is *band-limited* with *bandwidth* N, that is, $R_l^m = 0\,(l \geq N)$. Then, consider the "comb" function $s(\theta, \phi)$ with equiangular grid $(\Delta\theta, \Delta\phi) = (\pi/2N, 2\pi/2N)$,

$$s(\theta, \phi) = \frac{\sqrt{2\pi}}{2N} \sum_{j=0}^{2N-1} \sum_{k=0}^{2N-1} w_j \delta(\theta - \theta_j)\delta(\phi - \phi_k), \tag{10}$$

where $(\theta_j, \phi_k) = (\pi(j+1/2)/2N, 2\pi k/2N)$ are the sampling points on the sphere, and w_j are the weights of the points. We can compute the coefficients s_l^m of the comb function from definition in Eq. (3). For degree $l < 2N$, we obtain

$$s_l^m = \sum_{j=0}^{2N-1} w_j \sqrt{\frac{2l+1}{2}} P_l^0(\cos\theta_j)\delta_{m0}, \tag{11}$$

where the Kronecker delta $\delta_{ij} = 1$ if $i = j$, and $\delta_{ij} = 0$ if $i \neq j$. Here, we can uniquely choose the weight w_j so that $\sum_{j=0}^{2N-1} w_j P_l^0(\cos\theta_j) = \sqrt{2}\delta_{l0}$. Thus, the coefficients are described simply as $s_l^m = \delta_{l0}\delta_{m0}$ for degree $l < 2N$. Equivalently, the comb function is represented by the addition of $Y_0^0(\theta, \phi) = const.$ and higher-degree terms as

$$s(\theta, \phi) = 1 + \sum_{j \geq 2N} \sum_{|k| \leq j} s_j^k Y_j^k(\theta, \phi). \tag{12}$$

Then, from Eqs. (6) and (12), the product of the reflection kernel and the comb function is written as

$$\begin{aligned} &R(\theta, \phi) \cdot s(\theta, \phi) \\ &= R(\theta, \phi) + \sum_{l<N} \sum_{|m| \leq l} \sum_{j \geq 2N} \sum_{|k| \leq j} R_l^m s_j^k Y_l^m(\theta, \phi) Y_j^k(\theta, \phi), \end{aligned} \tag{13}$$

where degree $l < N$ because $R(\theta, \phi)$ is band-limited. The second term is known as *aliasing* introduced by discrete sampling. However, it is known that the product of the spherical harmonics $Y_l^m(\theta, \phi)Y_j^k(\theta, \phi)$ is represented as a linear combination of spherical harmonics with a degree greater than or equal to $|l - j|$. Accordingly, aliasing appears a degree greater than or equal to $|N - 2N| = N$ in this case. Therefore, for degree $l < N$, $R(\theta, \phi) \cdot s(\theta, \phi)$ is equal to $R(\theta, \phi)$, that is,

$$(R(\theta, \phi) \cdot s(\theta, \phi))_l^m = R_l^m. \tag{14}$$

Hence, the coefficients of the reflection kernel can be computed accurately by the Fourier transform of $R(\theta, \phi) \cdot s(\theta, \phi)$ as

$$R_l^m = \frac{\sqrt{2\pi}}{2N} \sum_{j=0}^{2N-1} \sum_{k=0}^{2N-1} w_j R(\theta_j, \phi_k) Y_l^m(\theta_j, \phi_k), \tag{15}$$

where the weight w_j are analytically given by

$$w_j = \frac{2\sqrt{2}}{2N} \sin\theta_j \sum_{n=0}^{N-1} \frac{1}{2n+1} \sin[(2n+1)\theta_j]. \tag{16}$$

4. Appearance Sampling of Real Objects Based on Sampling Theorem

The sampling theorem described in the previous section tells us the minimum number of sampling $2N \times 2N = 4N^2$ to compute spherical harmonics transformation of a band-limited function with bandwidth N. In this section, we consider the issues in defining the bandwidth of an object.

4.1. Convex Lambertian Surface

Let us start with the simplest case of convex Lambertian objects. It has been shown in previous studies that the first nine spherical harmonics with the order $l = 2$ are sufficient to capture more than 99% of the reflection energy of a convex Lambertian surface (Basri and Jacobs 2001; Ramamoorthi and Hanrahan 2001a,b).

Accordingly, we can consider that the function $R(\theta, \phi)$ is band-limited with bandwidth $N = 3$, and this results in $4N^2 = 36$ samplings of $R(\theta, \phi)$ necessary for correctly computing R_l^m. In other words, the coefficients R_l^m are given as the finite weighted sums of the function $R(\theta, \phi)$ sampled at an equiangular grid: $\theta_j = \frac{\pi(j+1/2)}{6}$ $(j = 0, \ldots, 5)$, $\phi_k = \frac{2\pi k}{6}$ $(k = 0, \ldots, 5)$. Namely, 36 input images of an object taken by moving a point light source to the directions specified with (θ_j, ϕ_k) on a sphere around the object are required to compute harmonic images of the object.

Note that what needs to be satisfied is not the number of samplings $(4N^2)$ of the function but the sampling intervals $(\Delta\theta = \pi/2N, \Delta\phi = 2\pi/2N)$ that this sampling can provide. For instance, even when a large number of input images of an object taken under a point light source are available, there is no guarantee that this set of images can produce correct harmonic images that can span a low-dimensional linear subspace representing the appearance of the object under arbitrary illumination unless those intervals are satisfied.

4.2. Complex Appearance Beyond Lambertian

Ramamoorthi and Hanrahan analytically derived the bandwidth of the reflection kernels of objects that have more complex appearances than convex Lambertian surfaces, such as the Phong reflection model and the Microfacet BRDF (Ramamoorthi and Hanrahan, 2001a).[5] For instance, this study shows the bandwidth of the Microfacet BRDF is approximately $N \approx \sigma^{-1}$. Thus, if the surface roughness of an object is even roughly predicted, it should help us to find the bandwidth of the reflection kernel of the object.

There are a large number of previous studies on BRDF measurements and databases that show the reflectance parameters of various kinds of surface materials (Ngan et al., 2005). This knowledge should be useful for estimating bandwidths of reflection kernels of various objects based on the analysis presented by Ramamoorthi and Hanrahan (2001a). For reference, a table that shows bandwidths of some example materials is provided in Table 1 based on the analysis in Ngan et al. (2005). In addition, the appearances of several materials are synthesized under a natural illumination condition from their harmonic images recovered by our proposed method.

Table 1. Bandwidth of example surface materials.

Material	Surface roughness	Bandwidth
acrylic-blue	0.0137	74
alum-bronze	0.0367	29
aventurnine	0.0145	70
black-oxidized-steel	0.19	7
black-obsidian	0.0239	43
black-plastic-soft	0.325	5
blue-rubber	0.276	5
dark-blue-paint	0.292	5
delrin	0.143	8
fabric	0.585	3
fruitwood	0.0924	12
gold-paint	0.214	6
green-metallic-paint	0.143	8
nickel	0.0424	25
nylon	0.0662	17
red-french-wax	0.13	9
red-oak	0.116	10
rose-quartz	0.0302	35
teflon	0.139	9

In Fig. 2, the synthesized appearances are compared with the ray-traced appearances of those objects: the first row shows the ray-traced images of the objects and the second row shows the synthesized results by our method using $2N \times 2N = 4N^2$ samplings of their appearances.

4.3. Discussion on Geometric Effects

Spherical harmonics have been used for efficient rendering of an object under low-frequency complex illumination. When an object contains a large quantity of high-frequency components in its reflection, the number of required bases may become very large. Geometric effects observed on an object surface such as cast shadows can be considered to be high-frequency components.

Sloan et al. experimentally showed that spherical harmonics were not efficient in synthesizing cast shadows seen under a very high-frequency lighting, e.g., a point light source, while diffuse and glossy inter-reflections were well represented with spherical harmonics of lower order even when the lighting contained very high frequency components (Sloan et al., 2002). In the context of inverse lighting, Okabe et al. showed that high frequency components of the appearance of an object surface could retain significant energy by taking the cast shadow on the object surface as well as its BRDF into account (Okabe et al., 2004).

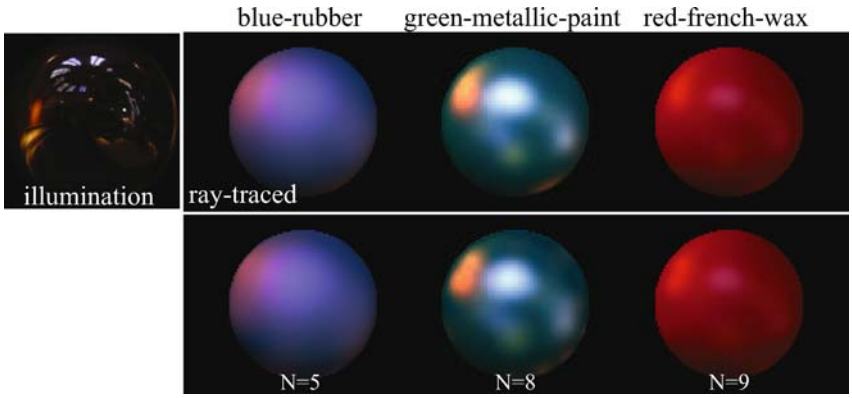

Figure 2. Synthesized images of spheres with different surface materials under natural illumination. The first row shows the ray-traced images of the objects and the second row shows the synthesized results using $2N \times 2N = 4N^2$ samplings of their appearances.

Recently, Ramamoorthi et al. provided an analysis of cast shadows for 3D textures based on canonical configurations of V-groove type structure (Ramamoorthi et al., 2005). It is interesting to extend their analysis to the task of appearance sampling of objects with complex shapes by considering other geometric configurations.

4.4. Experimental Results Using Point Light Source

We have tested the proposed approach using real images of several objects taken by moving a point light source to equiangular grid points defined by the sampling theorem.[6] For the sheep and Venus examples, since those objects have similar appearances to that of a Lambertian surface, 36 input images were taken under a point light source positioned at the equiangular grid points described in Section 4.1. For the fish example, since it has a more complex appearance, 144 input images, which is the limit of the hardware set-up used for acquiring input images, were taken under a point light source at equiangular grid points: $\theta_j = \frac{\pi(k+1/2)}{12}$, $\phi_k = \frac{2\pi k}{12}(j, k = 0, \ldots, 11)$. Based on the sampling theorem, coefficients R_l^m were computed up to the degree $l = 2$ from the 36 images, and up to the degree $l = 5$ from the 144 images, respectively.

The first nine harmonic images obtained from those input images are shown in Fig. 3. In spite of the given discrete sets of the appearances of the objects, the obtained harmonic images have complex and smooth shading that reflects the distribution of harmonic lights in both examples. We synthesize their appearance from the recovered harmonic images under several natural illumination conditions provided by high-dynamic range light probe measurements by Debevec (1998). In Fig. 4, the synthesized appearance changes dynamically depending on the characteristics of the illumination.

We also compare the synthesized appearance with the real appearance of those objects. In Fig. 5, the left column shows the real images of the objects taken under normal lighting conditions in our laboratory and the right column shows the synthesized appearance. The synthesized appearance of the objects resembles that of the objects in the real images, and this shows that the recovered harmonic images provide a good representation of the appearance of the objects. The shoulder of the plaster figure in the lower right image appears darker than that in the real image. This is due to severe cast shadows observed in the input images that correspond to the high-frequency components of the object's appearance.

5. Aliasing Caused by Insufficient Sampling

There is certainly a situation where it is difficult to predict the bandwidth of the reflection kernel of an object, or where only a limited number of samplings of the reflection kernel are obtainable due to the limitation of the hardware set-up used for acquiring input images. When samplings of the reflection kernel of an object are insufficient, the obtained coefficients suffer from aliasing, and this leads to undesirable artifacts, such as ringing in the reflection kernel reconstructed from those coefficients. Therefore, it is important to consider what kinds of artifacts we should expect when the function $R(\theta, \phi)$ has a lower or a higher bandwidth than N determined from the number of samplings $4N^2$ based on the sampling theorem.

Driscoll and Healy proved that the error in spherical harmonics transformation, generally known as aliasing, is confined to coefficients R_l^m of a degree greater than or equal to $|B - 2N|$, where B denotes the actual bandwidth of the function (Driscoll and Healy, 1994). This can be confirmed by replacing the bandwidth N of the reflection function with B in Eq. (13). From this, the following discussion is provided.

- In cases where the function has a bandwidth B lower than N ($B < N$), there is no aliasing for a degree less

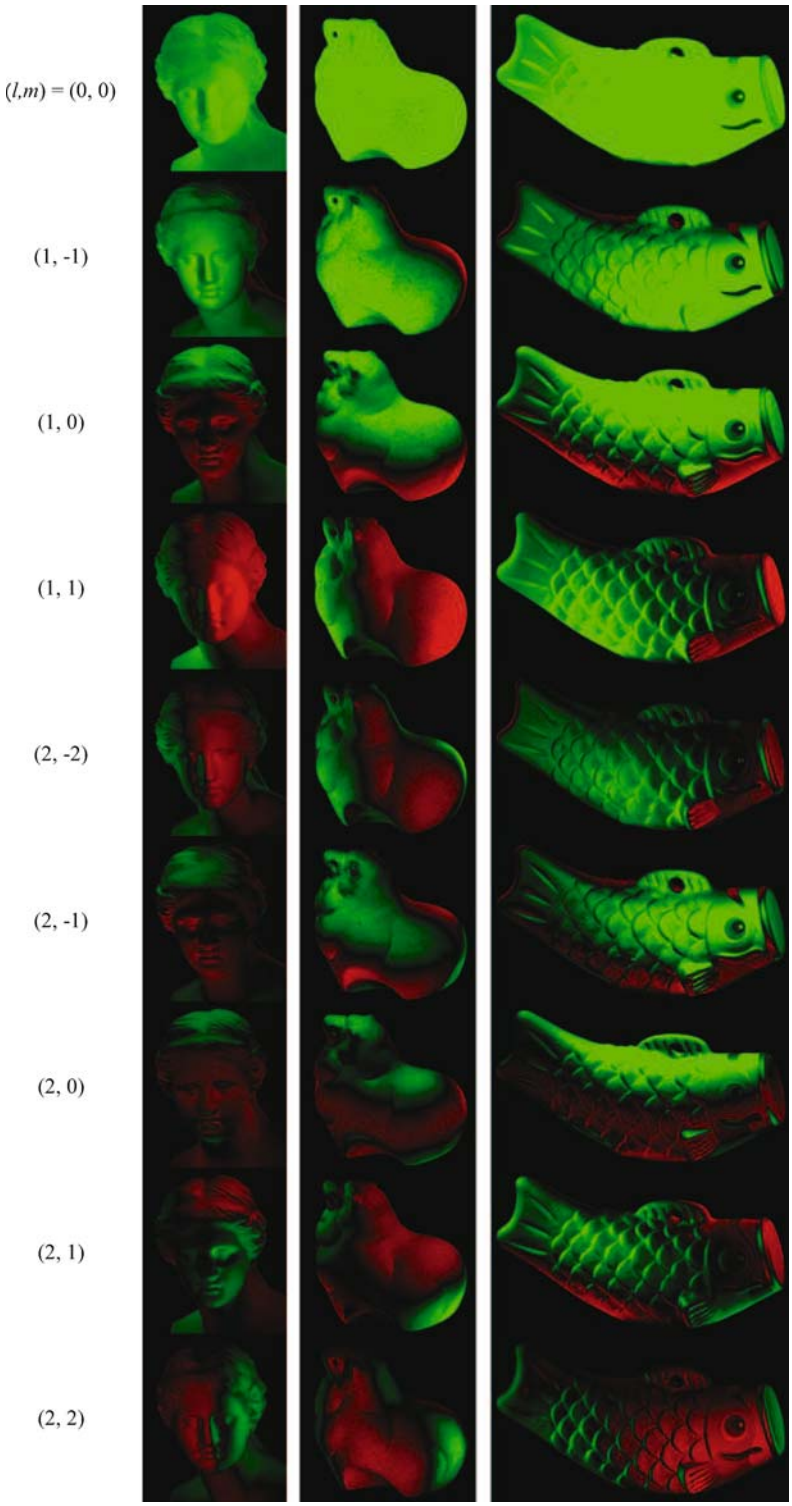

Figure 3. Obtained harmonic images: positive values are shown in green, and negative values are shown in red.

than $N + k$ for $B = N - k$. Since we compute coefficients R_l^m for $l < N$, those coefficients are correctly computed. In this case, all of the coefficients R_l^m for $B \leq l < N$ become 0.

- In cases where the function $R(\theta, \phi)$ has a bandwidth B higher than N ($B > N$), errors due to insufficient sampling of the function are confined to the coefficients of degree $l \geq N - k$ for $B = N + k$. In this case, the

Figure 4. Synthesized images of objects under natural illumination. The first column shows the illumination maps. The second, third, and forth columns show the synthesized appearance of the objects under the corresponding illumination maps.

coefficients R_l^m for $l < N - k$ degree are correctly computed. Therefore, the closer to B we select N, the smaller the errors in R_l^m we can expect.

In the next section, we consider an anti-aliasing framework for obtaining a set of correct basis images from an insufficient number of input images.

6. Anti-Aliasing Framework for Modeling Appearance Using Extended Light Sources

The sampling theorem states that the higher the frequency content of an object's appearance, the more input images are required to obtain a correct set of basis images. The number of input images required may become extremely large in the case of highly specular surfaces containing a large quantity of high frequency components in their reflection. Since the number of input images provided for modeling an object's appearance is usually limited, an anti-aliasing framework for obtaining a set of correct basis images from an insufficient number of object input images is needed.

We extend the method based on the sampling theorem further for reducing the artifacts due to aliasing, by substituting the extended light sources for a point light source to sample the reflection kernel of a real object. More specifically, in this section we investigate the effectiveness of using Extended Light Sources *(ELS)* for modeling the appearance of an object under varying illumination.

The use of ELS for modeling the shape and reflectance of an object was originally introduced by Nayar et al. (1990), where ELS was positioned around a target object to observe at least two measurements of non-zero specular intensities under the ELS for an object whose specular reflection component is considered to be very sharp and thus approximated by a delta function. This method then extracts the shape and reflectance properties of the

Figure 5. Comparison between real images and synthesized images under complex illumination.

object based on the hybrid reflection model proposed by the authors (Nayar et al., 1991). We extend their analysis further in the angular frequency domain so that the harmonic images of an object of arbitrary surface materials can be obtained without suffering from the aliasing caused by insufficient sampling of its appearance.

Extended light sources (*ELS*) may be constructed by illuminating a spherical diffuser with a point light source (Fig. 6).

The use of ELS brings the following three advantages:

Functioning as a low-pass filter. ELS have a radiance distribution that is similar to that of the Gaussian function. This enables extended sources to function as a low-pass filter when the reflection kernel of an object is sampled under ELS. From this, we are able to model its appearance without suffering from aliasing.

Adjustable bandwidth. The distribution of ELS can be adjusted by changing the distance from the diffuser to a point light source. This enables us to adjust the bandwidth of the ELS in the frequency domain.

Reducing saturation problem. When an object is illuminated by a point light source, image intensities from its specular reflection components often become much greater than those from its diffuse reflection components. Under ELS, the gap between the image intensities due to the specular and diffuse reflection components are narrowed (Nayar et al., 1990). This helps avoid saturation, so that we are able to observe both specular and diffuse reflection components in the same image.[7]

In the following sections, we consider the reflection kernel of an object sampled under ELS.

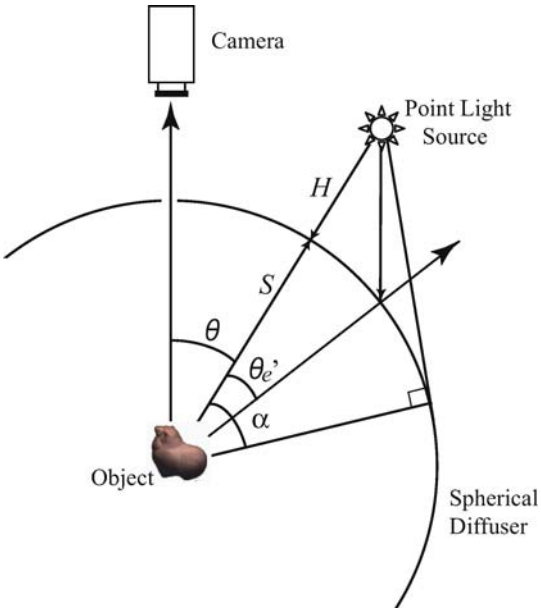

Figure 6. ELS are constructed by a spherical diffuser and a point light source (Nayar et al., 1990).

6.1. *Radiance Distribution of ELS*

First, the radiance distribution of ELS is provided. The radiance distribution of ELS is symmetric with respect to the point source direction, and therefore has no azimuth dependence around the point source direction. Accordingly, the radiance of the inner surface of the diffuser E may be represented as a function of the elevation angle θ'_e, that is $E(\theta'_e, \phi'_e) = E(\theta'_e)$. Here θ'_e represents the elevation angle defined with respect to the direction of the point light source (Fig. 6).

Then, $E(\theta'_e)$ are computed from the analytic formula derived by Nayar et al. (1990) as

$$E(\theta'_e) = \frac{CP[(S+H)\cos\theta'_e - S]}{\left[(S+H-S\cos\theta'_e)^2 + (S\sin\theta'_e)^2\right]^{\frac{3}{2}}}, \quad (17)$$

where P denotes the radiance of the point source and C is a constant representing the proportionality between the irradiance of the outer surface of the diffuser to the radiance of its inner surfaces. As illustrated in Fig. 6, S is the radius of the spherical diffuser and H is the distance from the diffuser's surface to the point light source.[8] Here the surface points on the diffuser within the range of $\theta'_e < \alpha$ can receive energy from the point light source, and the effective range α is determined by the relationships between S and H as $\alpha = \cos^{-1}(\frac{S}{S+H})$.

6.2. *Reflection Kernel Sampled Under ELS*

Next, let us consider a reflection kernel $R(\theta, \phi)$ sampled as an observed brightness of an object surface when it is illuminated by ELS whose center is located at the direction (θ, ϕ).

Since the radiance of the ELS are distributed over the spherical surface of the diffuser, the modified reflection kernel seen under ELS, denoted as $R'(\theta, \phi)$, is determined by computing the integral of the scene radiance resulting from the illumination of the entire surface of the extended source as

$$R'(\theta,\phi) = \int_0^{\pi}\int_0^{2\pi} R\left(M_\theta^\phi(\theta'_e, \phi'_e)\right) E(\theta'_e)\sin\theta'_e \mathrm{d}\theta'_e \mathrm{d}\phi'_e, \quad (18)$$

where $M_\theta^\phi(\cdot)$ is a rotation operator that rotates the distribution of the ELS $E(\theta'_e)$ so that its center $(\theta'_e = 0)$ is located in the direction (θ, ϕ). In other words, the modified reflection kernel $R'(\theta, \phi)$ is determined by convolving the original reflection kernel $R(\theta, \phi)$ with the radiance distribution of the ELS $E(\theta'_e)$ (Fig. 7).

$R(M_\theta^\phi(\theta'_e, \phi'_e))$ and $E(\theta'_e)$ in Eq. (18) can be expanded as a linear combination of spherical harmonics, and Eq. (18) is rewritten in terms of spherical harmonics as

$$R'(\theta,\phi) = \sum_{l=0}^{\infty}\sum_{m=-l}^{l} R_l^m E_l \sqrt{\frac{4\pi}{2l+1}} Y_l^m(\theta,\phi). \quad (19)$$

A mathematical derivation of Eq. (19) is shown in the Appendix. R_l^m and E_l represent the coefficients in the spherical harmonic expansion of the reflection kernel

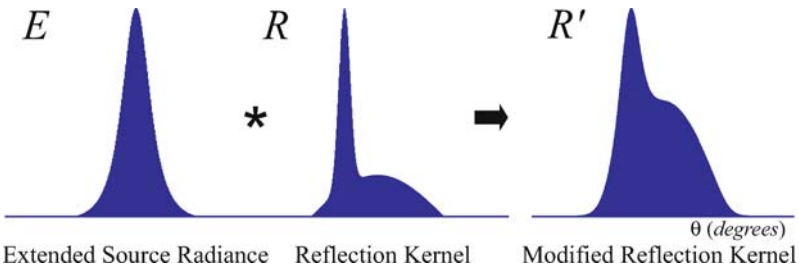

Figure 7. Modified Reflection Kernel obtained by convolving original reflection kernel $R(\theta, \phi)$ with distribution of ELS $E(\theta'_e)$.

$R(\theta, \phi)$ and ELS $E(\theta'_e)$, respectively, and the term $\sqrt{\frac{4\pi}{2l+1}}$ tells us how to compute a rotated spherical harmonic of the same order l.

The important point to note in Eq. (19) is that the modified reflection kernel $R'(\theta, \phi)$ is computed as a product of the coefficient R_l^m and E_l. From Eqs. (2) and (19), the spherical harmonic coefficients R'^m_l of the modified reflection kernel $R'(\theta, \phi)$ become

$$R'^m_l = R_l^m E_l \sqrt{\frac{4\pi}{2l+1}}. \tag{20}$$

This indicates that the modified reflection kernel $R'(\theta, \phi)$ is band-limited with the lower bandwidth between $R(\theta, \phi)$ and $E(\theta'_e)$. Fortunately, it is not difficult to adjust the bandwidth of the ELS.

6.3. *Adjusting Bandwidth of ELS*

As noted by Nayar et al. (1990), ELS have a distribution similar to that of the Gaussian function, and their distribution and effective range α are determined by the radius S of a spherical diffuser and the distance H from the diffuser surface to a point light source as defined in Eq. (17). In other words, the closer the point light source is positioned to the diffuser, the narrower its range α becomes. This property of ELS enables us to specify its bandwidth.

The Fourier transform of the Gaussian function is known to lead to another Gaussian function in the frequency domain. Therefore, convolution of a function with the Gaussian function in the spatial domain is equivalent to low pass filtering, since it leads to multiplying the Fourier coefficients of the function by the Gaussian function in the frequency domain. In addition, the standard deviation σ_f of the Gaussian function in the frequency domain is known to become inversely proportional to the standard deviation σ_s of the Gaussian function in the spatial domain. That is $\sigma_f = \frac{1}{\sigma_s}$.

Similarly, we can safely say that the spherical convolution of a function with the Gaussian function defined on a unit sphere also results in low-pass filtering since it is equivalent to multiplying its spherical harmonics coefficients with a half-Gaussian function.[9]

To see how the bandwidth of ELS changes depending on their α values, we synthetically provide several radiance distributions of ELS with different α values from

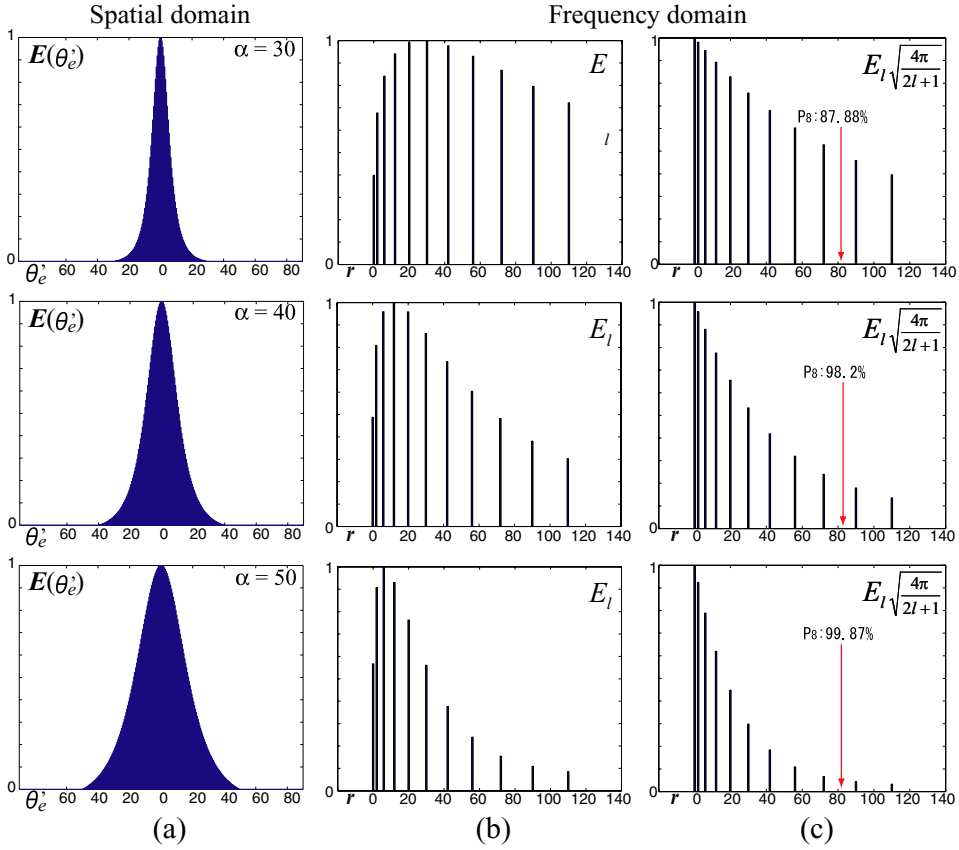

Figure 8. Distribution of ELS: (a) spatial domain, (b) and (c) frequency domain.

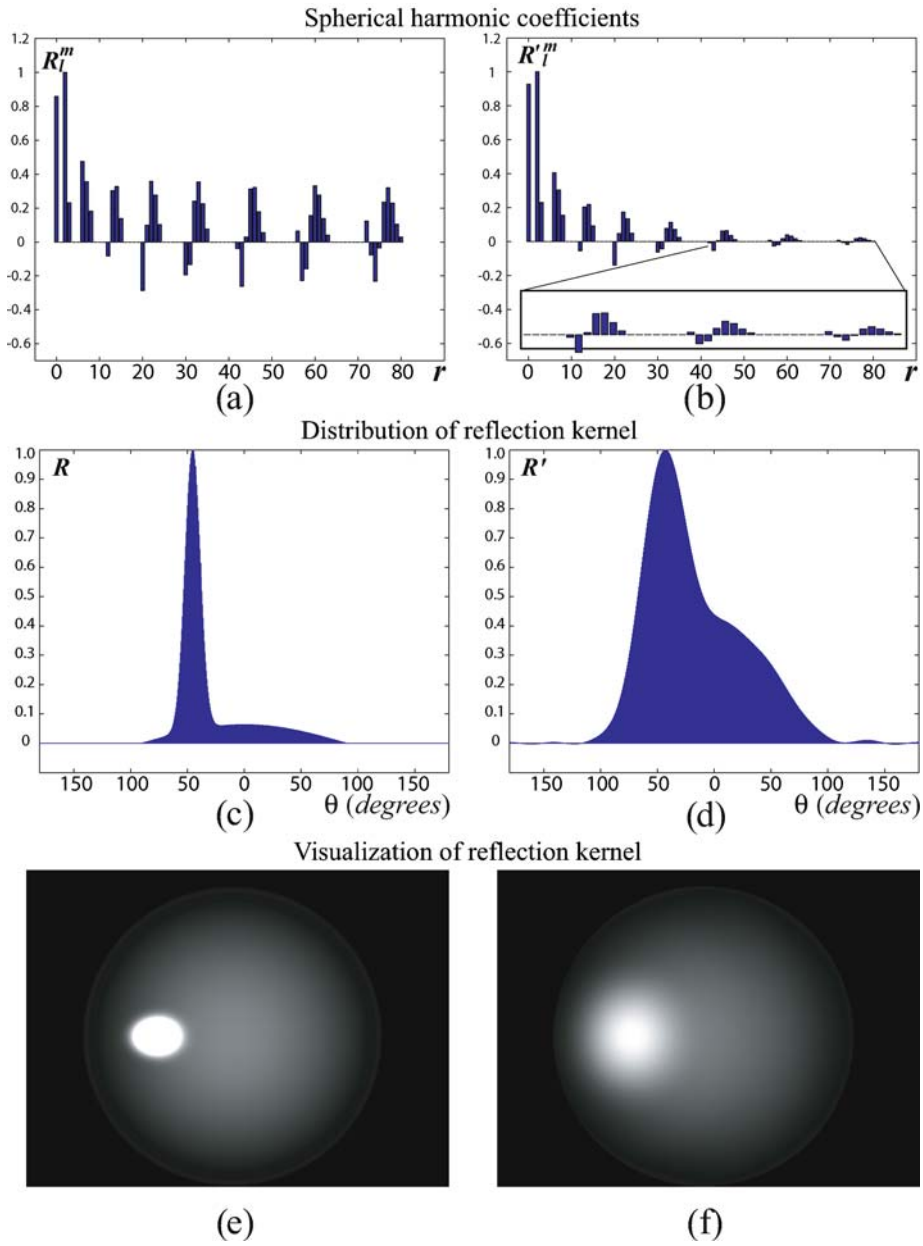

Figure 9. Glossy gray paper: original reflection kernel (left), and obtained modified reflection kernel (right).

Eq. (17). The spatial distribution and corresponding α of those extended sources and their coefficients E_l are shown in Fig. 8. In this figure, spherical harmonic coefficients for given degree l and order m are represented using a single index $r = l^2 + l + m$. The horizontal axis represents the index r, and the vertical axis represents the coefficients E_l in (b) and the coefficients including the rotation terms $E_l\sqrt{\frac{4\pi}{2l+1}}$ in (c).

In each graph in Fig. 8(c), the left side of a red arrow corresponds to the coefficients up to the degree $l = 8$. The energy captured by spherical harmonics up to the degree $l = 8$, denoted as P_8, are also computed by sums of the squares of their respective coefficients divided by the total squared energy of the transformed function. In this figure, we clearly see that P_8 becomes closer to 100% as their α values increase from 30 to 50 degrees. Especially in the case of $\alpha = 50$ degrees, more than 99% of the total energy is captured by the spherical harmonics up to the degree $l = 8$, so it is reasonable to assume that the extended source generated with $\alpha = 50$ degrees is band-limited with a bandwidth $l = 8$. As shown in this example, the bandwidth of ELS can be set by adjusting their effective range α.

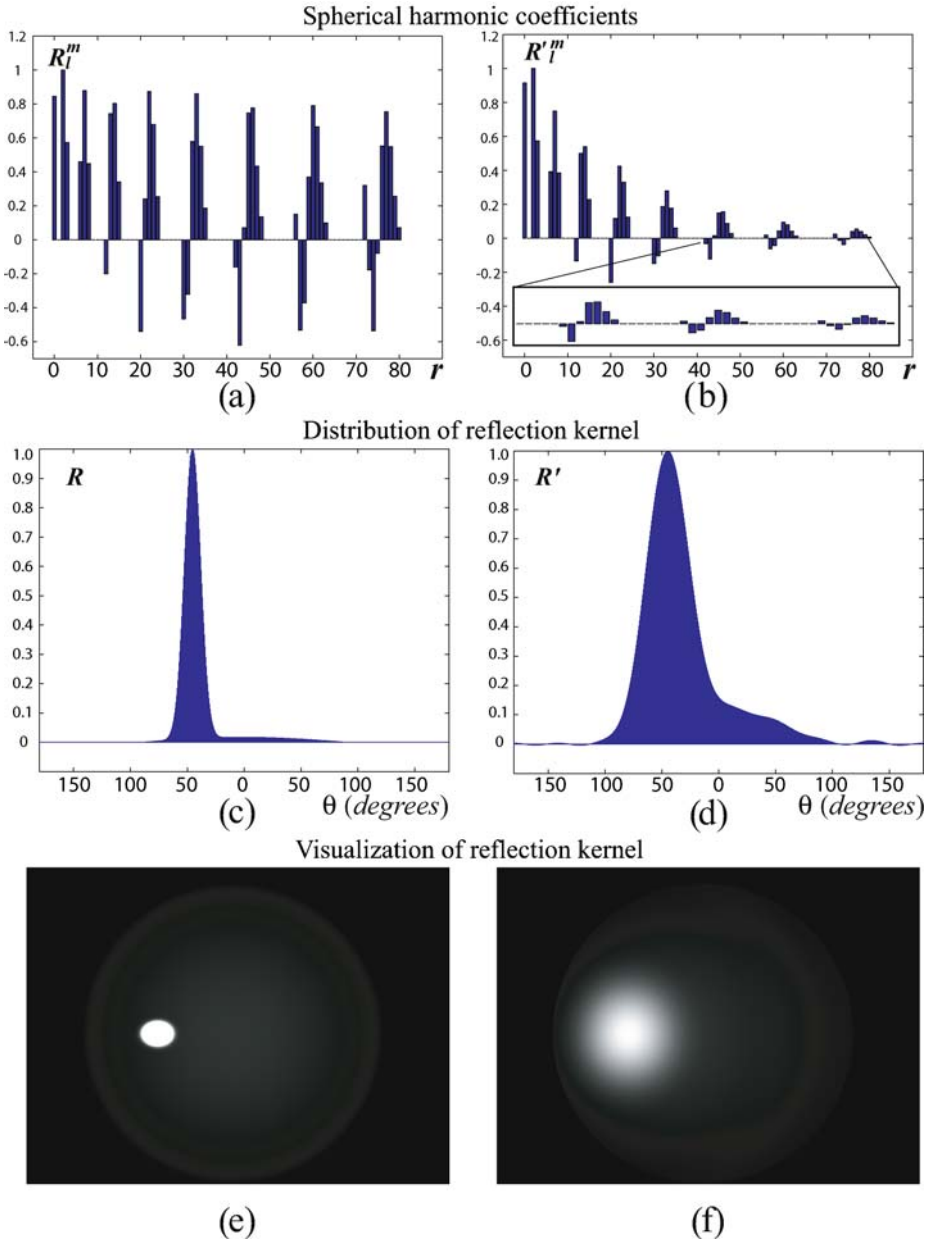

Figure 10. Lightly brushed aluminum: original reflection kernel (left), and obtained modified reflection kernel (right).

6.4. Modeling Appearance by Using ELS

Based on the analysis in the previous section, we propose a novel scheme for sampling the reflection kernel of an object by ELS with a properly adjusted range α.

Here we employ an efficient sampling scheme proposed by Mohlenkamp (1999) that requires fewer samplings of the function than the sampling theorem described in Section 3.1 does. This sampling scheme is derived to sample a function that is ensured to be band-limited with a particular bandwidth. If the function is not band-limited with the specified bandwidth, the under-sampled portion of the function appears in its lower frequencies in a complex way and tends to have a larger effect on the computed coefficients than the aliasing we discussed before.

Let us consider the case where the appearance of an object is observed under ELS whose bandwidth is properly adjusted to B. The modified reflection kernel $R'(\theta, \phi)$ of the object then becomes band-limited with the same bandwidth B as the ELS, and this enables us to use this efficient sampling scheme. This sampling scheme tells us that the spherical harmonics transformation of a

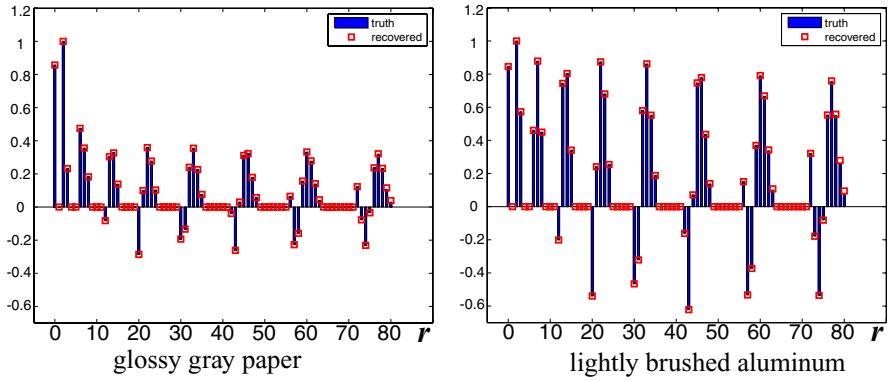

Figure 11. Recovered reflection kernel: $R_l^m = R'^m_l/(E_l\sqrt{\frac{4\pi}{2l+1}})$.

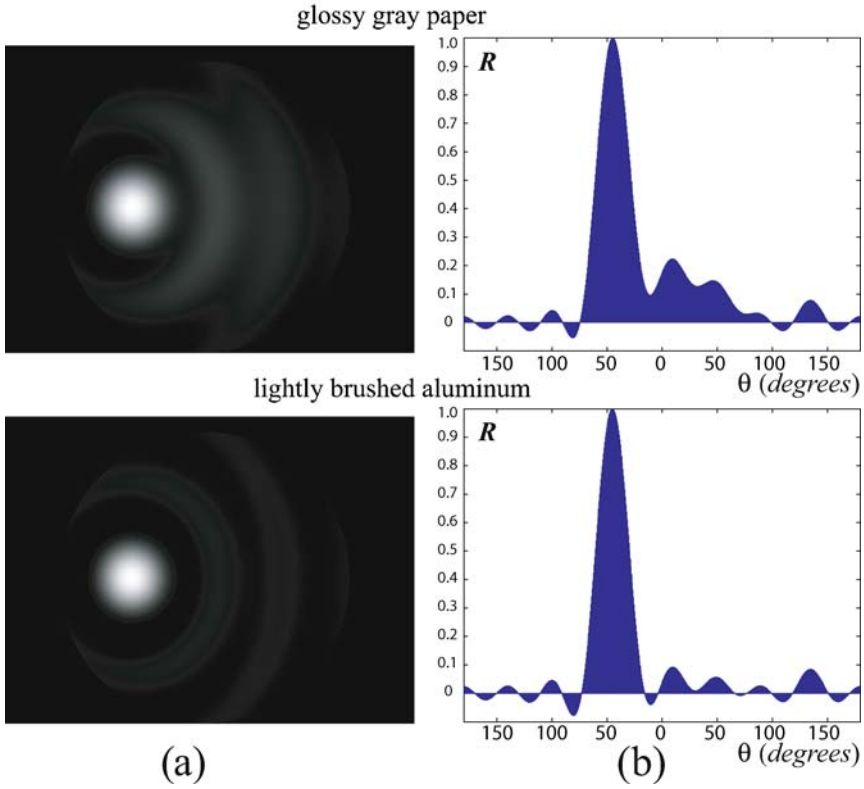

Figure 12. Reconstructed reflection kernel from coefficients R_l^m of original reflection kernel up to degree $l = 8$.

band-limited function with a bandwidth B ($R'^m_l = 0\,(l \geq B)$), can be computed by weighted sums of $2B^2 - B$ sampled function values based on a Gaussian quadrature (Press et al., 1988) as

$$R'^m_l = \frac{2\pi}{2B-1}\sum_{j=0}^{B-1}\sum_{k=0}^{2B-2} w_j R'(\theta_j, \phi_k) Y_l^m(\theta_j, \phi_k), \tag{21}$$

where the weights w_j are those of the Gaussian quadrature, θ_j are the Gaussian nodes in $\cos\theta$, and $\phi_k = \frac{2\pi_k}{(2B-1)}$ are equally sampled in azimuth (Mohlenkamp, 1999; Okabe et al., 2004).

7. Experimental Results Using ELS

7.1. *Synthetic Data*

The reflection kernel $R(\theta, \phi)$ of several surface materials are synthetically provided based on the Ward isotropic reflection model (Ward, 1992) with the known reflection parameters shown in Table 2: K_d and K_s are constants for

Table 2. Reflection parameters.

Material	K_d	K_s	σ
glossy gray paper	.29	.083	.082
lightly brushed aluminum	.15	.19	.088

the diffuse and specular reflection components, respectively, and σ is the standard deviation of the surface slope. Here the surface normal and viewing direction for the reflection kernel are set at the direction ($\theta_n = 0, \phi_n = 0$) and ($\theta_o = 45, \phi_o = 0$), respectively.

The ELS used in this experiment are generated with $\alpha = 50$ degrees, whose bandwidth is equivalent to $B = 9$. This makes the modified reflection kernel $R'(\theta, \phi)$ band-limited with $B = 9$. Accordingly, the spherical harmonic coefficients R'^m_l of the band-limited function $R'(\theta, \phi)$ were obtained from a properly sampled discrete set of function values (153 samplings for $B = 9$ in Eq. (21)).

The right columns in Figs. 9 and 10 show the obtained reflection kernel for glossy gray paper and lightly brushed aluminum surfaces, respectively. Figures 9 and 10(b) show the computed coefficients R'^m_l, and (d) and (f) show the distribution of $R'(\theta, \phi)$ reconstructed from the obtained R'^m_l in Eq. (2) up to the degree $l = 8$.[10]

For reference, the left columns of these figures show the coefficients and distribution of the original reflection kernel $R(\theta, \phi)$. Figures 9 and 10(a) show its coefficients computed from 100000 samplings of $R(\theta, \phi)$, and (c) and (e) show its distribution computed by substituting the reflection parameters into the Ward reflection model.

Comparing (a) with (b), while the magnitude of the coefficients is different because of the multiplication with the coefficients of the ELS whose distribution is similar to that of a half Gaussian function, the recovered R'^m_l go up and down in the same manner as R^m_l if we see their distributions locally.

In addition, the coefficients R^m_l of the original reflection kernel can be recovered by substituting E_l and the obtained R'^m_l into Eq. (20), if necessary. Figure 11 shows the recovered R^m_l compared with the ground truth coefficients. Here, the solid lines show the ground truth coefficients and the squares show the estimated ones. We can see that the recovered coefficients are almost the same as the ground truth coefficients, and it can be said from this that the proposed method successfully estimated the coefficients of the original reflection kernel up to the degree defined by the sampling intervals, without suffering from aliasing caused by insufficient sampling of its function values.

In Figs. 12(a) and (b), we also provide the low-frequency appearance of the original reflection kernel for reference by substituting the coefficients R^m_l up to degree $l = 8$ into Eq. (6). In other words, all coefficients with the index $l > 8$ of R^m_l are truncated in this case.

Comparing Figs. 9 and 10(f) with the low-frequency appearance of the original reflection kernel in Fig. 12(a), the modified reflection kernel reconstructed by our method provides a good representation of the low-frequency appearance of the original reflection kernel, although a high-frequency appearance, such as the specular peak in (e), is blurred due to the approximation of the original reflection kernel up to the degree $l = 8$.

It is worth noting that almost no undesirable artifacts appear in the reconstructed reflection kernel $R'(\theta, \phi)$ in Figs. 9 and 10(f). This shows that the proposed method succeeded in computing the coefficients R'^m_l of the modified reflection kernel from the 153 discrete samplings of $R'(\theta, \phi)$ without suffering from aliasing due to insufficient sampling of its appearance.

In contrast, as Westin et al. pointed out (Westin et al., 1992), simply truncating all coefficients R^m_l with $l > 8$ resulted in undesirable artifacts, such as ringing in the reconstructed reflection. This ringing is called the Gibbs phenomenon and is shown in Fig. 12(a) and (b).

In order to avoid the Gibbs phenomenon, Westin et al. progressively reduced the magnitude of the coefficients according to a half Gaussian distribution of an empirically

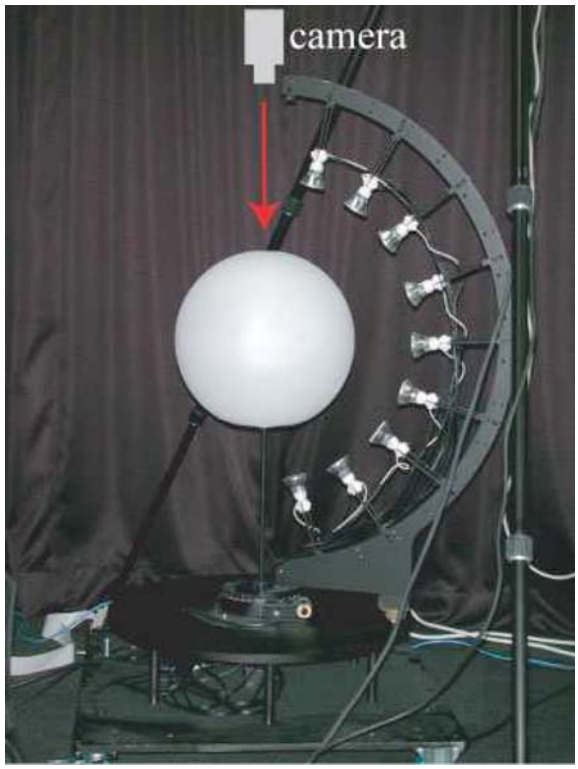

Figure 13. Experimental setup: 9 halogen lamps were positioned at Gaussian nodes in elevation, and an array of these light sources were mounted on a turntable and rotated around the spherical diffuser by $\phi_k = \frac{2\pi_k}{(18-1)}$, $(k = 0, \ldots, 16)$ degrees in azimuth.

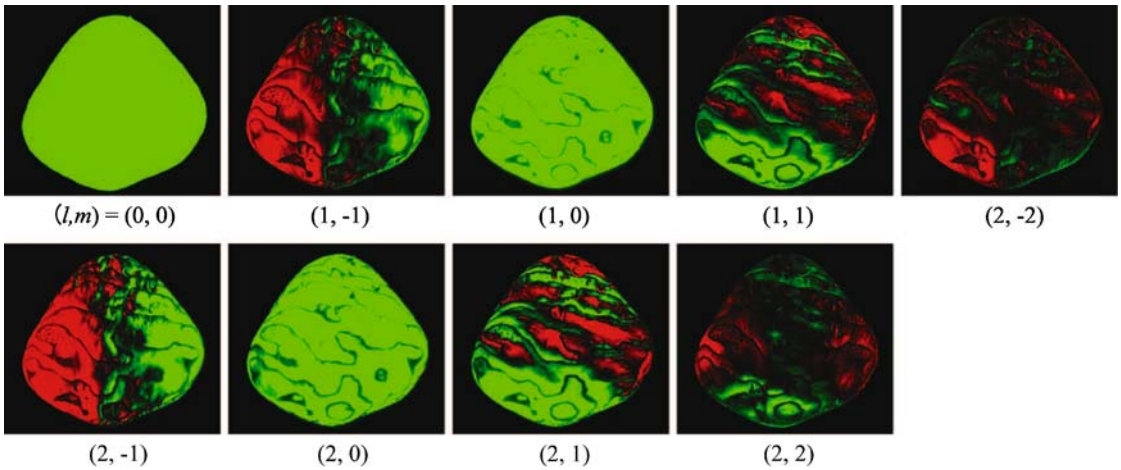

(a) Obtained harmonic images

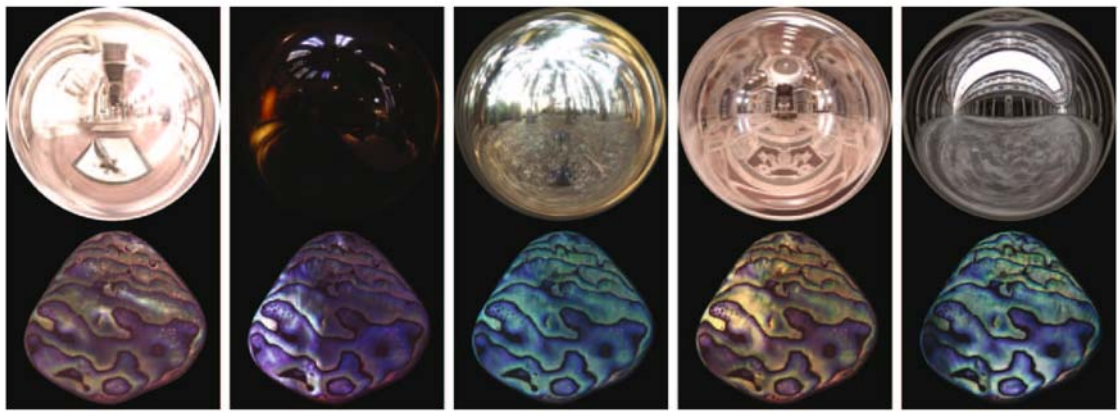

(b) Synthesized images of shellfish under natural Illumination conditions

Figure 14. (a) Obtained harmonic images and (b) Synthesized images under natural illumination conditions.

determined width. Fortunately, the coefficients of the ELS used in our method have a distribution that is similar to that of a half Gaussian distribution, as shown in Fig. 8.

It follows from this that the use of ELS is desirable not only as a method of modifying the original reflection kernel to be band-limited, but also for reducing the number of artifacts caused by the truncation of the coefficients with index $l \geq B$ of the original reflection kernel.

7.2. *Real Data*

Real images of abalone shellfish were taken under the physically constructed ELS apparatus shown in Fig. 13. Abalone shellfish are famous for their interesting structural colors, which alter greatly depending on the viewing direction and illumination conditions.

In this set-up, 9 halogen lamps were positioned at Gaussian nodes in elevation, and an array of these light sources were mounted on a turntable and rotated around the spherical diffuser (an acrylic globe with a diameter of 35 cm) by $\phi_k = \frac{2\pi_k}{(18-1)}, (k = 0, \ldots, 16)$ degrees in azimuth. Here the number of point light sources in elevation indicates that a modified reflection kernel has to be band-limited with $B = 9$. Accordingly the distance between the diffuser and the point light sources was adjusted so that the bandwidth of the constructed ELS was set to $B = 9$.

In total, 153 input images of the abalone shellfish were taken to sample its reflection kernel at each grid point (θ_j, ϕ_k). Then coefficients R'^m_l of this reflection kernel were computed up to the degree $l = 8$ by substituting the observed reflection kernel $R'(\theta_j, \phi_k)$ into Eq. (21). The first nine harmonic images obtained by our method are shown in Fig. 14(a).

Figure 14(b) shows the appearance of the abalone shellfish synthesized from Eq. (9) under natural illumination conditions provided as high-dynamic range light

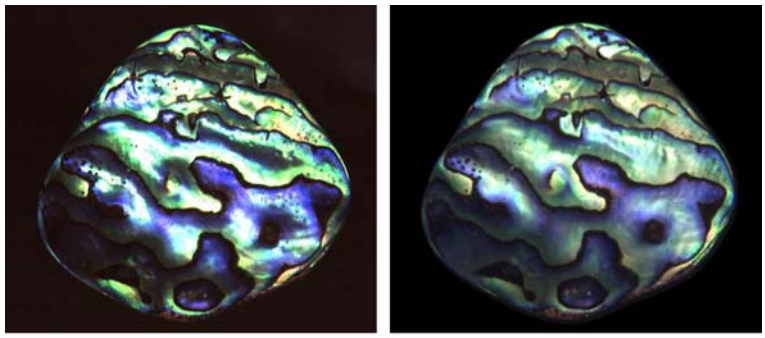

Figure 15. Comparison between real images and synthesized images under complex illumination.

probe measurements by Debevec (1998). In this figure, the synthesized appearance of the abalone shellfish significantly changes depending on the characteristics of the given illumination distributions, and this shows that the complex appearance of its structural colors are well represented by a set of basis images obtained by our method.

In addition, the synthesized appearance of the shellfish is compared with its real appearance as seen under a normal lighting condition in our laboratory in Fig. 15. Here coefficients L_l^m of this lighting condition are computed from an omni-directional image of the scene taken by a camera with a fish-eye lens. In this figure, the synthesized appearance highly resembles the real image. As has been noted before, in the case of a highly specular surface, image intensities from specular reflection components tend to be much greater than those from diffuse reflection components. This is the reason why image intensities in the real image become saturated in some specular regions.

In general, the limited dynamic range of an image taken with one shutter speed makes it difficult to model the appearance of highly specular surfaces. In contrast, the use of ELS contributes to the reduction of the high contrast between image intensities from both specular and diffuse components. This helps us to observe and model the appearance of highly specular surfaces from images taken at a single shutter speed.

8. Conclusions

We have presented a novel method for analytically obtaining a set of basis images of an object for arbitrary illumination from the input images of the object taken under a set of realizable light sources, such as a point light source or extended light sources. The main contribution of our work is that we have shown that a set of lighting directions can be determined for sampling images of an object depending on the spectrum of the object's BRDF in the angular frequency domain, such that a set of harmonic images can be analytically obtained based on the sampling theorem on spherical harmonics.

This study further considered the issue of aliasing caused by insufficient sampling of an object's appearance. In particular, we have demonstrated the effectiveness of using Extended Light Sources (ELS) for modeling the appearance of an object under varying illumination and described three merits of using ELS: (1) ELS have the ability to function as a low-pass filter for sampling objects' appearance, so basis images of an object can be obtained without suffering from aliasing caused by insufficient sampling of its reflection kernel, (2) ELS can reduce the high contrast between image intensities from both specular and diffuse components. This helps us observe and model the appearance from images taken at a single shutter speed, and (3) ELS can minimize undesirable artifacts resulting from the truncation of spherical harmonic coefficients of higher degrees.

These advantages helped provide basis images of an object from a limited number of samplings of its appearance. Our method can adequately synthesize the appearance of an object up to a certain frequency. However, objects of high bandwidths, such as a mirror illuminated by a point light source, are difficult to be adequately modeled. A future research direction of this work would be to integrate other modeling techniques with the objective of recovery of an object's original reflection kernel. Also, it would be interesting to investigate the potential of other types of light sources serving as a low-pass filter when the appearance of an object is sampled under them.

Appendix

A modified reflection kernel $R'(\theta, \phi)$ is described in Eq. (18) as

$$R'(\theta, \phi) = \int_0^{\pi} \int_0^{2\pi} R\left(M_\theta^\phi(\theta'_e, \phi'_e)\right) E(\theta'_e) \sin\theta'_e \mathrm{d}\theta'_e \mathrm{d}\phi'_e.$$

$R(M_\theta^\phi(\theta'_e, \phi'_e))$ and $E(\theta'_e)$ can be expanded as a linear combination of spherical harmonics:

$$E(\theta'_e) = \sum_{n=0}^{\infty} E_n Y_n^0(\theta'_e) \tag{22}$$

$$R\left(M_\theta^\phi(\theta'_e, \phi'_e)\right) = \sum_{l=0}^{\infty} \sum_{m=-l}^{l} R_l^m Y_l^m\left(M_\theta^\phi(\theta'_e, \phi'_e)\right), \tag{23}$$

where R_l^m and E_n denote the coefficients in their spherical harmonic expansion. Then, a rotation formula for spherical harmonics is given by Ramamoorthi and Hanrahan (2001a) as $Y_l^m(M_\theta^\phi(\theta'_e, \phi'_e)) = \sum_{m'=-l}^{l} D_{m,m'}^l(\theta) e^{Im\phi} Y_l^{m'}(\theta'_e, \phi'_e)$, where the term $e^{Im\phi}$ considers the rotation about ϕ, and the matrix D^l tells us how to compute a rotated spherical harmonic as a linear combination of all the spherical harmonics of the same order l.

By substituting (22) and (23), (18) becomes

$$R'(\theta, \phi) = \sum_{n=0}^{\infty} \sum_{l=0}^{\infty} \sum_{m=-l}^{l} \sum_{m'=-l}^{l} R_l^m E_n D_{m,m'}^l(\theta) e^{Im\phi} \times \int_0^{\pi} \int_0^{2\pi} Y_l^{m'}(\theta'_e, \phi'_e) Y_n^0(\theta'_e) \sin\theta'_e \mathrm{d}\theta'_e \mathrm{d}\phi'_e. \tag{24}$$

Then the orthonormality of the spherical harmonics tells us

$$\int_0^{\pi} \int_0^{2\pi} Y_l^{m'}(\theta'_e, \phi'_e) Y_n^0(\theta'_e) \sin\theta'_e \mathrm{d}\theta'_e \mathrm{d}\phi'_e = \delta_{ln}\delta_{m'0},$$

and therefore

$$R'(\theta, \phi) = \sum_{n=0}^{\infty} \sum_{l=0}^{\infty} \sum_{m=-l}^{l} \sum_{m'=-l}^{l} R_l^m E_n D_{m,m'}^l(\theta) e^{Im\phi} \delta_{ln}\delta_{m'0}. \tag{25}$$

Finally, from the characteristics of Kronecker delta ($\delta_{ij} = 1$ if $i = j$, and $\delta_{ij} = 0$ if $i \neq j$), the modified reflection kernel is obtained.

$$R'(\theta, \phi) = \sum_{l=0}^{\infty} \sum_{m=-l}^{l} R_l^m E_l D_{m,0}^l(\theta) e^{Im\phi} \tag{26}$$

Here one can see (Ramamoorthi and Hanrahan, 2001b; Driscoll and Healy, 1994) that $D_{m,0}^l(\theta) e^{Im\phi} = \sqrt{\frac{4\pi}{2l+1}} Y_l^m(\theta, \phi)$, thus

$$R'(\theta, \phi) = \sum_{l=0}^{\infty} \sum_{m=-l}^{l} R_l^m E_l \sqrt{\frac{4\pi}{2l+1}} Y_l^m(\theta, \phi). \tag{27}$$

Notes

1. In the context of texture synthesis, Malzbender et al. took the alternative approach of modeling the luminance dependencies of a texture on the lighting directions with biquadratic polynomials (Malzbender et al., 2001).
2. Harmonic images have also been used for the purpose of efficient rendering of an object under complex illumination (Ramamoorthi and Hanrahan, 2001c; Sloan et al., 2002).
3. In this study, we consider spherical harmonics in a real form.
4. Note that we can determine $R(\theta, \phi)$ only up to some unknown scaling factor, so it is reasonable to treat a point light source as having unit radiance.
5. Ramamoorthi and Hanrahan (2002) is also a good reference to get insights into the bandwidth of reflection kernels of various types of objects in a CURET database. This work discusses appropriate sampling resolutions to model the appearance of those objects based on their experiments as well.
6. *Surface Reflectance Sampler* by TechnoDream21 corporation was used for obtaining the input images of the objects.
7. The use of the multiplexed illumination proposed by Schechner et al. (2003) is also effective in reducing this dynamic range problem of capturing both diffuse and specular reflection.
8. This formula is based on the condition that the spherical diffuser is ideal and thus incident energy is equally scattered in all directions.
9. Gaussian distribution with a half range with positive values.
10. The (d) figures show $R'(\theta, \phi)$ scanned in the line of $\{\theta|0 \leq \theta \leq \pi/2\}$, $\{\phi|0$ or $\pi\}$, and (f) show the upper half of the reflection kernel visualized in a polar coordinate system with radius indicating $\{\theta|0 \leq \theta \leq \pi/2\}$, and an angle indicating $\{\phi|0 \leq \phi < 2\pi\}$.

References

Basri, R. and Jacobs, D. 2001. Lambertian reflectance and linear subspaces. In *Proc. IEEE Int. Conf. Computer Vision 01*, pp. 383–389.

Debevec, P. 1998. Rendering synthetic objects into real scenes: Bridging traditional and image-based graphics with global illumination with high dynamic range photography. In *Proc. SIGGRAPH 98*, pp. 189–198.

Driscoll, J. and Healy Jr., D. 1994. Computing Fourier transforms and convolutions on the 2-sphere. *J. Advanced in Applied Mathematics*, 15:202–250.

Epstein, R., Hallinan, P., and Yuille, A. 1995. 5+/−2 eigenimages suffice: An empirical investigation of low-dimensional lighting models. In *Proc. IEEE Workshop on Physics-Based Modeling in Computer Vision*, pp. 108–116.

Georghiades, A., Kriegman, D., and Belhumeur, P. 1998. Illumination cones for recognition under variable lighting: Faces. In *Proc. IEEE Conf. Computer Vision and Pattern Recognition*, pp. 52–59.

Georghiades, A., Kriegman, D., and Belhumeur, P. 2001. From few to many: Generative models for recognition under variable pose and illumination. *IEEE Trans. Pattern Analysis and Machine Intelligence*, 23(6):643–660.

Hallinan, P. 1994. A low-dimensional representation of human faces for arbitrary lighting conditions. In *Proc. IEEE Conf. Computer Vision and Pattern Recognition*, pp. 995–999.

http://healpix.jpl.nasa.gov/

Lee, K.C., Ho, J., and Kriegman, D. 2001. Nine points of light: Acquiring subspaces for face recognition under variable lighting. In *Proc. IEEE Conf. Computer Vision and Pattern Recognition 01*, pp. 519–526.

Malzbender, T., Gelb, D., and Wolters, H. 2001. Polynomial texture maps. In *Proc. SIGGRAPH 01*, pp. 519–528.

Mohlenkamp, M.J. 1999. A fast transform for spherical harmonics. *J. Fourier Analysis and Applications*, 5(2/3):159–184.

Murase, H. and Nayar, S. 1995. Visual learning and recognition of 3-D objects from appearance. *Int. J. Computer Vision*, 14(1):5–24.

Nayar, S.K., Ikeuchi, K., and Kanade, T. 1991. Surface reflection: Physical and geometrical perspectives. *IEEE Trans. Pattern Analysis and Machine Intelligence*, 13(7):611–634.

Nayar, S.K., Ikeuchi, K., and Kanade, T. 1990. Determining shape and reflectance of hybrid surfaces by photometric sampling. *IEEE Trans. Robotics and Automation*, 6(4):418–443.

Nishino, K., Zhang, Z., and Ikeuchi, K. 2001. Determining reflectance parameters and illumination distribution from sparse set of images for view-dependent image synthesis. In *Proc. IEEE Int. Conf. Computer Vision 01*.

Ngan, A., Durand, F., and Matusik, W. 2005. Experimental analysis of BRDF models. In *Proc. the Eurographics Symposium on Rendering*, pp. 117–226.

Okabe, T., Sato, I., and Sato, Y. 2004. Spherical harmonics vs. haar wavelets: Basis for recovering illumination from cast shadows. In *Proc. IEEE Conf. Computer Vision and Pattern Recognition*, pp. I-50–57.

Press, W.H., Flannery, B.P., Teukolsky, S.A., and Vetterling, W.T. 1988. *Numerical Recipes in C: The Art of Scientific Computing*. Cambridge University Press: Cambridge.

Ramamoorthi, R. and Hanrahan, P. 2001a. A signal-procession framework for inverse rendering. In *Proc. SIGGRAPH 01*, pp. 117–128.

Ramamoorthi, R. and Hanrahan, P. 2001b. On the relationship between radiance and irradiance: Determining the illumination from images of a convex lambertian object. *J. Optical Society of America A*, 18(10):2448–2459.

Ramamoorthi, R. and Hanrahan, P. 2001c. An efficient representation for irradiance environment maps. In *Proc. SIGGRAPH 01*, pp. 497–500.

Ramamoorthi, R. and Hanrahan, P. 2002. Frequency space environment map rendering. In *Proc. SIGGRAPH 02*, pp. 517–526.

Ramamoorthi, R., Koudelka, M., and Belhumeur, P. 2005. Fourier theory for cast shadows. *IEEE Trans. PAMI*, 27(2):288–295.

Sato, I., Okabe, T., Sato, Y., and Ikeuchi, K. 2003. Appearance sampling for obtaining a set of basis images for variable illumination. In *Proc. IEEE Int. Conf. Computer Vision*, pp. 800–807.

Sato, I., Okabe, T., Sato, Y., and Ikeuchi, K. 2005. Using extended light sources for modeling object appearance under varying illumination. In *Proc. IEEE Int. Conf. Computer Vision*, pp. 325–332.

Schechner, Y., Nayar, S., and Belhumeur, P. 2003. A theory of multiplexed illumination. In *Proc. IEEE Int. Conf. Computer Vision*, pp. 808–815.

Schroder, P. and Sweldens, W. 1995. Spherical Wavelets: efficiently representing functions on the sphere. In *Proc. SIGGRAPH 95*, pp. 161–172.

Shim, K. and Chen, T. 2004. Efficient representation of lighting patterns for image-based relighting. In *Proc. Picture Coding Symposium*.

Shashua, A. 1997. On photometric issues in 3D visual recognition from a single image. *Int. J. Computer Vision*, 21:99–122.

Sloan, P., Kautz, J., and Snyder, J. 2002. Precomputed radiance transfer for real-time rendering in dynamic, low-frequency lighting environments. In *Proc. SIGGRAPH 02*, pp. 527–536.

Ward, G.J. 1992. Measuring and modeling anisotropic reflection. In *Proc. SIGGRAPH 92*, pp. 265–272.

Westin, S., Arvo, J., and Torrance, K. 1992. Predicting reflectance functions from complex surfaces. In *Proc. SIGGRAPH 92*, pp. 255–264.

Yuille, A., Snow, D., Epstein, R., and Belhumeur, P. 1999. Determining generative models of objects under varying illumination: Shape and albedo from multiple images using SVD and integrability. *Int. J. Computer Vision*, 35(3):203–222.

Zhang, L. and Samaras, D. 2003. Face recognition under variable lighting using harmonic image exemplars. *IEEE Conf. Computer Vision and Pattern Recognition*, I:19–25.

Zhao, L. and Yang, Y. 1999. Theoretical analysis of illumination in PCA-based vision systems. *Pattern Recognition*, 32:547–564.